PCCP

PAPER

View Article Online
View Journal | View Issue

Cite this: *Phys. Chem. Chem. Phys.*, 2024, **26**, 5922

Experimental and computational studies of the optical properties of 2,5,8-tris(phenylthiolato)heptazine with an inverted singlet–triplet gap†

Daniel Blasco, *[a] Rinat T. Nasibullin,[b] Rashid R. Valiev,[b] Miguel Monge,[a] José M. López-de-Luzuriaga[a] and Dage Sundholm *[b]

Received 29th October 2023,
Accepted 30th January 2024

DOI: 10.1039/d3cp05242g

rsc.li/pccp

Photophysical properties of the three-fold symmetric 2,5,8-tris(phenylthiolato)heptazine molecule (**1**) are studied from combined experimental and computational viewpoints. The intense blue photoemission of **1** in the solid state and in toluene solution is proposed to have a fluorescent origin on the basis of a relatively short emission lifetime and no detectable triplet decay. Calculations at correlated *ab initio* levels of theory also show that **1** has a large inverted singlet–triplet (IST) gap, a non-vanishing spin–orbit coupling matrix element between the first excited singlet and triplet states, and a fast intersystem crossing rate constant that leads to singlet population from the higher-lying triplet state. The IST gap implies that the first excited singlet state is the lowest excited one, agreeing with the measured fluorescent behaviour of **1**. IST gaps are also obtained for the oxygen-containing (**2**) and selenium-containing (**3**) analogues of **1** at the ADC(2) level of theory, but not for the tellurium one (**4**). Calculations of the magnetically induced current density demonstrate that the heptazine core of **1** is globally non-aromatic due to the alternation of carbon and nitrogen atoms along its external rim.

1 Introduction

Heptazine (1,3,4,6,7,9,9*b*-heptaazaphenalene, tri-*s*-triazine, or cyamelurine in older texts; see Fig. 1, left) is a fused planar phenalenyl tricycle featuring a central nitrogen atom and alternating carbon and nitrogen atoms along the external rim. The high rigidity of the phenalenyl core, and the precise accumulation of the electron density on the peripheral nitrogen atoms, give rise to remarkable properties that make heptazine derivatives useful in diverse applications *e.g.*, as building blocks for MOFs and COFs, photocatalysts, or electroluminescent species for organic light-emitting diodes (OLEDs).[1] In particular, the optical properties of heptazine are well known and there are many examples of intensely luminescent heptazine derivatives,[1] some of which even display thermally-activated delayed fluorescence (TADF).[2–6]

The lowest-energy excited singlet (S_1) and triplet (T_1) states of heptazine have the same orbital composition consisting of a localized set of atom-range multiple resonances (MR) from the HOMO, located on the six electron-rich peripheral nitrogen atoms, to the LUMO, on the carbon and central nitrogen atoms (see Fig. 1, right).[7] The character of these excitations is almost insensitive to corner functionalization (atomic positions 2, 5, and 8), even when the substituent is a heavy metal such as gold.[8] The small HOMO–LUMO overlap minimizes the exchange integral leading to a small energy difference between S_1 and T_1 [ΔE_{ST}, calculated as $\Delta E_{ST} = E(S_1 \leftarrow S_0) - E(T_1 \leftarrow S_0)$].[9]

By performing calculations at different levels of theory, several research groups have recently demonstrated that the energy order of S_1 and T_1 in heptazine is unexpectedly inverted (IST, see Fig. 2).[7,8,10–22] The violation of Hund's maximum multiplicity rule[23] by non-alternating polycyclic polyenes is not a new phenomenon. A more stable S_1 with respect to T_1 was observed for the symmetric forms of propalene, pentalene, heptalene,[24] and, more recently, in isopyrene.[25–27] However, far from just being a scientific curiosity, IST is expected to give rise to a new kind of light-emitting molecules, the so-called fifth generation of emitters with applications in OLED devices.[28,29]

[a] *Departamento de Química, Instituto de Investigación en Química (IQUR), Universidad de La Rioja, Madre de Dios 53, 26006, Logroño, Spain. E-mail: daniel.blascos@unirioja.es*
[b] *Department of Chemistry, Faculty of Science, University of Helsinki, P. O. Box 55 (A. I. Virtasen aukio 1), FIN-00014, Helsinki, Finland. E-mail: dage.sundholm@helsinki.fi*

† Electronic supplementary information (ESI) available: Emission spectrum of molecule **1** in the solid state at 78 K, transient photoluminescence spectra of molecule **1**, molecular orbital contributions to the most intense transitions of molecules **1–4**, streamlines of the MIC pathways of molecule **1**, selected bond lengths and angles of molecules **1–4**, Cartesian coordinates of molecules **1–4**. See DOI: https://doi.org/10.1039/d3cp05242g

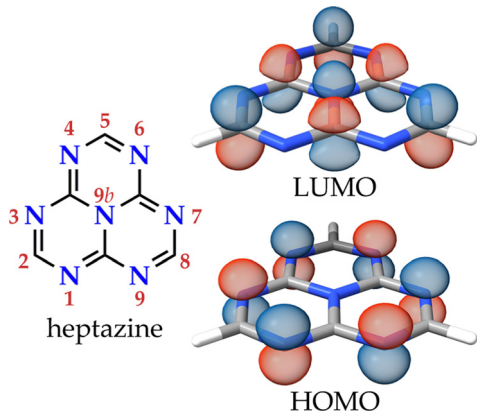

Fig. 1 The molecular structure of heptazine with the canonical numbering of the atomic positions and the HOMO and LUMO orbitals.

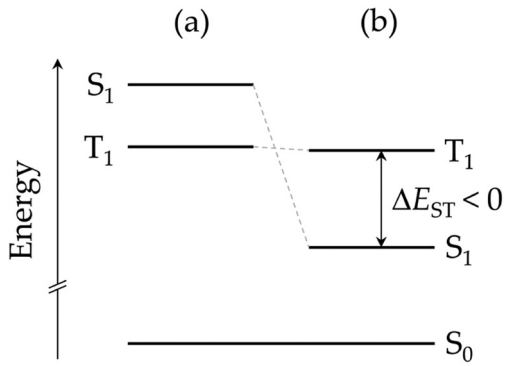

Fig. 2 Energy diagram of the first excited states of a molecule (a) obeying Hund's multiplicity rule, and (b) with an inverted singlet–triplet gap.

The singlet–triplet inversion is expected to eliminate the need of thermal activation for achieving maximum external quantum efficiency. It also supresses the triplet decay channel, overcoming potential bimolecular annihilation processes that ordinary TADF emitters suffer from due to the long lifetime of the excited states, which are detrimental to the performance and stability of OLED devices.

The origin of IST is attributed to dynamic spin polarization effects of the first excited state,[24,30–32] which are accounted for at configuration interaction (CI) levels including double excitations. For a given active orbital space, Pauli's exclusion principle restricts the number of possible doubly-excited triplet configurations with respect to the number of doubly-excited singlet ones. When this extra dynamic spin polarization stabilization of S_1 exceeds the exchange energy, ΔE_{ST} becomes negative.[7,24,30] Thus, a proper description of the IST needs either single or multireference correlated wavefunction-based (*ab initio*) computational levels that accurately capture contributions from double excitations. These methods, in virtue of an improved description of the electronic structure, are computationally expensive and resource penalties preclude a widespread usage, justifying the use of cheaper but reliable approximate computational levels such as the approximate second-order coupled-cluster (CC2) and algebraic diagrammatic construction of second order [ADC(2)] methods.[33–37]

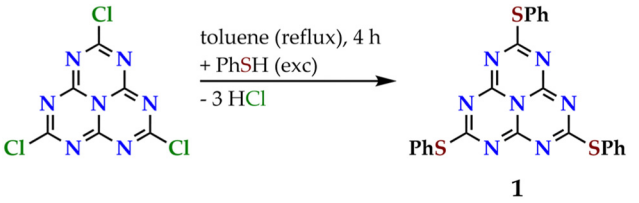

Fig. 3 Synthesis of molecule **1**.

Despite the increasing plethora of potential IST molecules identified by high-throughput virtual screenings,[10,17,26,38] there are still very few experimental studies of their photophysical properties.[7,10,13] In their seminal paper from 2022, Aizawa *et al.* proposed a decreasing trend of the delayed fluorescence lifetime component with decreasing temperature as a conclusive experimental proof of the so-called heptazine-type delayed fluorescence arising from IST.[10] However, we believe that the paucity and non-homogeneity of the available experimental data precludes a generalization of the photophysical behaviour of IST molecules. Thus, it is mandatory to continue gathering experimental data from molecules for which IST gaps are computationally detected, to gain a more complete picture of the actual behaviour and performance of these promising molecules.

Here, we report a thorough experimental study of the photophysical properties of 2,5,8-tris(phenylthiolato)heptazine (molecule **1**, see Fig. 3), which is identified to have a large inverted singlet–triplet gap at several *ab initio* correlated levels of theory. We show that the completely symmetrical derivatives of heptazine, which are excluded at the first stage of virtual screenings due to their vanishing $S_1 \leftarrow S_0$ oscillator strengths, can also be efficient IST emitters thanks to vibronic coupling. Besides, some of the measurements are performed on pure powder samples, a state that had not been considered in previous studies. We have focused on ether-like derivatives of heptazine due to their relative ease of synthesis and introduction of structural modifications in the pending moieties. Posern *et al.* synthesized a family of symmetric heptazine arylthio- (aryl = phenyl, *p*-tolyl, *p*-chlorophenyl, *p*-methoxyphenyl, 2-naphthyl, 1-methyltetrazyl) and phenylselenoethers starting from 2,5,8-trichloroheptazine, and studied their thermal stability. X-ray single-crystal structures were determined for the phenylthiolato and phenylselenolato derivatives as mesitylene (1,3,5-trimethylbenzene) solvates, revealing a three-fold symmetry axis and a staggered conformation of the phenyl planes with respect to the heptazine one. Besides, the title molecule **1** was identified as photoemissive in chloroform solution (λ_{em} at 552 nm with a λ_{ex} of 288 nm). Galmiche *et al.* proposed a new route to heptazine arylthioethers starting from the more soluble 2,5,8-tris(3,5-diethylpyrazolyl)heptazine and presented a more complete study of the photophysical properties of molecule **1**. Interestingly, the authors noted that there is a weak absorption band at low energies in all heptazine

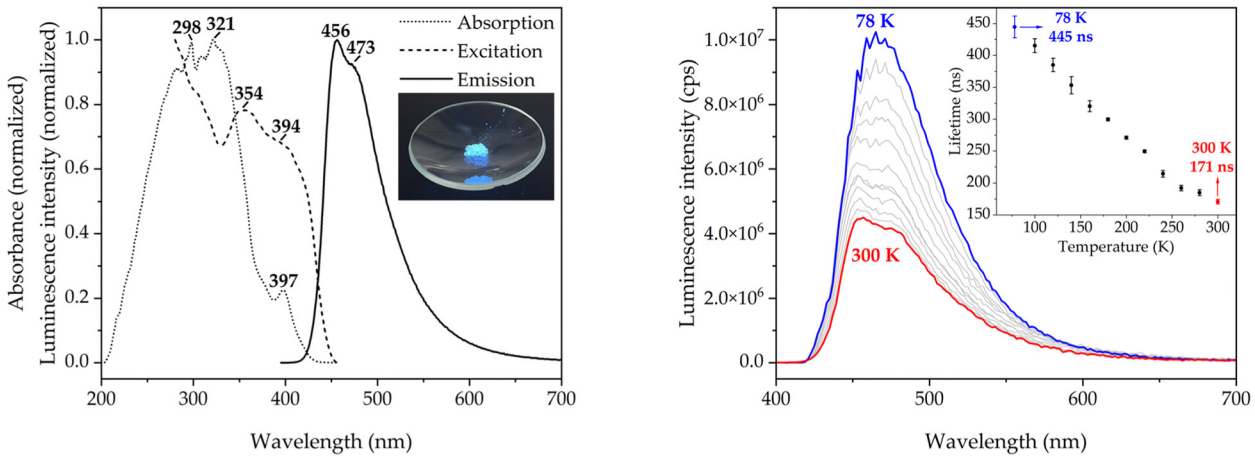

Fig. 4 (Left) The absorption (dotted line), the excitation (dashed line), and the emission (solid line) spectra of molecule 1 in the solid state (inset, solid illuminated by light with a λ_{ex} of 365 nm). (Right) The emission spectra for a λ_{ex} of 375 nm and average lifetimes in the solid state of molecule 1 (inset) for the same λ_{ex} at temperatures ranging from 78 K (blue line) to 300 K (red line) in steps of 20 K (grey lines).

derivatives they studied. The band was assigned with time-dependent density functional theory (TD-DFT) calculations to a symmetry-forbidden $S_1 \leftarrow S_0$ transition in the heptazine core.

The synthesis of **1** is described in Section 2.1 and in more detail in the Experimental Section 4. The experimental studies of the photophysical properties are discussed in Section 2.2, which is followed by computational characterization in Section 2.3 that comprises calculations of photophysical properties, the magnetically induced current density of **1**, and calculation of optical properties of related compounds where the S atoms are replaced by O (**2**), Se (**3**) or Te (**4**). The main results are summarized in the Conclusions Section 3.

2 Results and discussion

2.1 Synthesis of molecule 1

Molecule **1** was prepared by the nucleophilic attack of an excess of phenylthiol to 2,5,8-trichloroheptazine in refluxing toluene, in a similar way as previously reported (see Fig. 3).[39] The reaction gives rise to a mixture of the desired trisubstituted product with the disubstituted one and other unidentified byproducts, that are separated by flash column chromatography.[3] The identity and purity of **1** was assessed by $^{13}C\{^1H\}$ NMR. Molecule **1** is obtained as a white solid displaying intense blue photoluminescence (see inset in Fig. 4, left). The other spectroscopic measurements accord with the already published data.[3,39]

2.2 Photophysical studies

The optical properties of molecule **1** in the solid state, which have not been reported before, are discussed below (see Fig. 4). The diffuse reflectance (DR) UV-vis spectrum of **1** in potassium bromide mull (dotted line in Fig. 3, left) shows a structured asymmetric band centered at 300 nm. The low-energy edge of the band has a well-defined absorption band at 397 nm, which corresponds to the symmetry-forbidden $S_1 \leftarrow S_0$ transition (*vide infra*). The excitation and emission spectra at room temperature (dashed and solid lines in Fig. 4, left, respectively) are also examined. The emission spectrum features a single band with maxima at 456 and 473 nm and a broad tail in the green-to-yellow visible region, which is macroscopically observed as bright blue photoluminescence. The structure of the emissive excited state is not heavily distorted as indicated by the small Stokes shift of 3451 cm^{-1}. More interestingly, the spectral profile of the excitation spectrum resembles the low-energy edge of the absorption spectrum, including the energies of the maxima, which suggests that there is a spin-allowed excitation to the singlet manifold. The transient photoluminescence decay data was fitted to a sum of up to three exponential functions. The emission lifetime was calculated as an average weighted by the relative amplitudes of the exponentials (see Experimental Section 4 and the ESI†). The average emission lifetime of 171 ns at 300 K is unexpectedly long due to the symmetry-prohibited transition from the S_1 state. The absolute photoluminescence quantum yield (PLQY) of 0.33 is high, but not as high as that of HAP-3TPA of 0.91 (6 wt% embedded in a solid film), which is state-of-the-art.[6]

The emission spectrum and average lifetimes were also measured at low temperature (see Fig. 4, right and the ESI†). The emission intensity nearly triples upon cooling to 78 K as the restriction of vibrational motion disfavors non-radiative deactivations. The vibronic structure of the ground state is also revealed in the emission profile (see Fig. S1, ESI†). The energy difference between consecutive vibronic peaks is roughly 300 cm^{-1}, which is of the same size as the calculated energy of the out-of-plane vibration of the nitrogen atoms of the heptazine core (see Fig. S2, ESI†). The average emission lifetime at 78 K of 445 ns is about a factor of 2.5 longer than the one of 171 ns measured at 300 K indicating the influence of excited vibrational motion on the relaxation of S_1. However, it is still fast as compared to other relaxation channels. There is no evidence of participation of the triplet state at 78 K, precluding phosphorescent or TADF behavior.

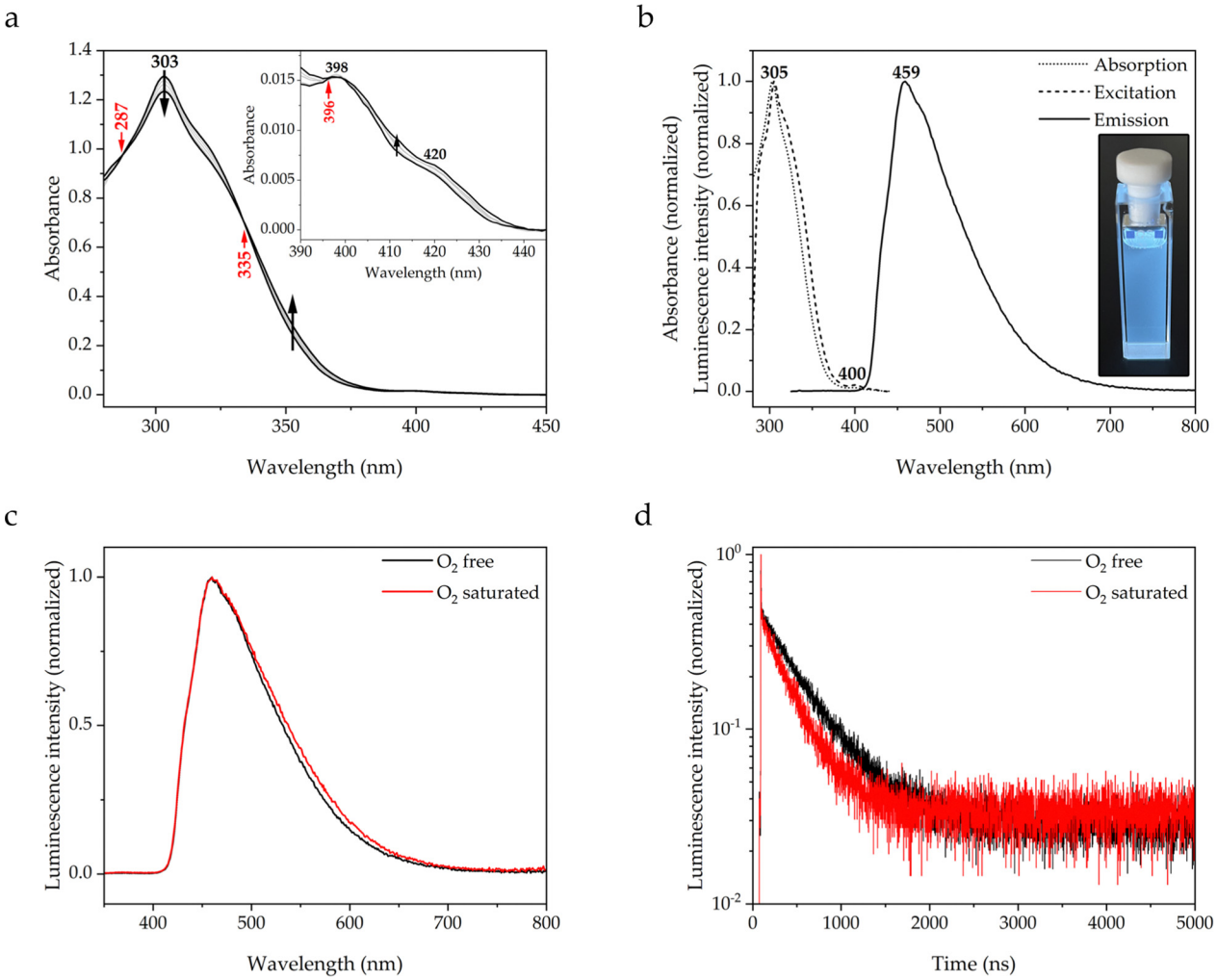

Fig. 5 (a) The absorption spectrum of molecule 1 in a 32 μM toluene solution at temperatures ranging from 20 to 70 °C in steps of 10 °C. (b) The absorption (dotted line), the excitation (dashed line), and the emission (solid line) spectra of molecule 1 in a 32 μM toluene solution (inset, solution illuminated by light with a λ_{ex} of 365 nm). (c) Superimposition of the normalized emission spectrum of molecule **1** in the absence (black line) and presence (red line) of molecular oxygen. (d). Superimposition of the normalized transient photoluminescence decay of molecule **1** in the absence (black line) and presence (red line) of molecular oxygen.

The photophysical properties of molecule **1** have also been measured in toluene solution (see Fig. 5), which was not considered in the study of Galmiche *et al.*[3] The UV-vis spectrum (see Fig. 5a) shows a structured absorption at 303 nm similar to the one observed by DR-UV-vis. A structured spectral trace corresponding to the $S_1 \leftarrow S_0$ transition is again observed around 410 nm, in line with the findings of Galmiche *et al.* for other solvents[3] (see Introduction Section 1). The spectrum has been measured at different temperatures in the 20 °C to 70 °C range. The spectral profile is slightly modified upon heating, whereas the absorption energies do apparently not depend on the temperature since the position of the maximum is not shifted. Notably, the absorbance of the spectral trace increases. Since the $S_1 \leftarrow S_0$ transition is symmetry-forbidden, a thermally-prompted increase of the promoting vibrational motion breaks the molecular symmetry and relaxes the prohibition rule, thus increasing the absorbance. The photoemissive properties have been measured in the absence and presence of molecular oxygen, which is a well-known quencher of luminescence *via* collisional energy transfer and formation of singlet oxygen. Besides that long-lived excited states are sensitive to the presence of molecular oxygen, it can also form an exciplex with the excited emitter molecule and thereby contribute to the luminescence quenching.[40]

Molecule **1** is extremely luminescent in solution, exhibiting intense blue emission with a PLQY of 0.71 even at μM concentrations (see Fig. 5b). The emission profile resembles the one in the solid state, with a maximum at 459 nm and a tail up to 700 nm, with a long emission lifetime of 462 ns. As expected, the presence of oxygen in solution leads to a drastic drop in the emission intensity, which is reflected in a shortening of the lifetime to 316 ns and a decrease in the PLQY to 0.38. However, it is noteworthy that the emission in not completely quenched, what would be expected if it were of phosphorescent nature.

Table 1 Photophysical properties of molecule **1**. Wavelengths (λ) are given in nm, lifetimes (τ) are given in ns, and the absolute photoluminescence quantum yield (φ)

Molecule	λ_{abs}	λ_{em} (λ_{ex})	τ	ϕ (λ_{ex})
Solid state, 300 K	295, 321, 397	456 (354)	171 ± 4	0.33 (374)
Solid state, 78 K	—[a]	472 (354)	445 ± 17	—[a]
Toluene, O_2 free	303, 398, 418	459 (306)	462 ± 2	0.71 (290)
Toluene, O_2 saturated	303, 398, 418	459 (306)	316 ± 2	0.38 (290)

[a] Presently we do not have instrumentation to measure these values.

Moreover, the spectral profiles are virtually indistinguishable without loss of vibronic fine structure (see Fig. 5c). This demonstrates that the triplet state is not populated at room temperature, since no part of the spectrum originates from triplet decay. The transient photoluminescence decay data shows monoexponential behaviour over the whole considered time range (see Fig. 5d and Fig. S5, ESI†). The longer lifetime and higher PLQY of **1** in solution than in the solid state, irrespective of the absence or presence of oxygen, suggest the formation of π-stacked exciplexes with toluene molecules, what is supported by the observation of π-stacks with mesitylene molecules in the crystal state.[39] The photophysical properties of molecule **1** are summarized in Table 1.

2.3 Computational studies

2.3.1 Excitation energies and spectra. The electronic origin of the absorption spectrum of molecule **1** in the solid state is assigned with the aid of TD-DFT/PBE0/def2-TZVP calculations on an optimized model extracted from the X-ray structure of 2,5,8-tris(phenylthiolato)heptazine (see Fig. 6, top).[39] TD-DFT is not the method of choice for modeling the excitation landscape of IST molecules, as it is unable to capture dynamic spin polarization except when using frequency-dependent kernels or double hybrid functionals.[14] However, the high number of needed vertical transitions makes the usage of more reliable correlated wavefunction methods computationally expensive. An overlay of the solid-state absorption and excitation spectra with the energetically lowest symmetry-allowed singlet excitations of molecule **1** is plotted in Fig. 6, bottom. The excitation energies of the symmetry-forbidden $S_1 \leftarrow S_0$ and $T_1 \leftarrow S_0$ transition are also marked for illustrative purposes. The orbital contributions to the most intense transitions are reported in Table 2 and plotted in the ESI.†

There are two pairs of doubly-degenerate transitions of high intensity at 289 and 241 nm. They are considerably blue-shifted with respect to the absorption maxima. The energy mismatch may be due to stabilizing packing effects in the solid state, that are not taken into account in the calculation. The $S_6 \leftarrow S_0$ and $S_7 \leftarrow S_0$ transitions correspond to charge transfers from the HOMO−1 and HOMO−2, mainly located on the sulfur atoms of the pending phenylthiolate substituents with smaller contributions on the phenyl rings and the peripheral nitrogen atoms of the heptazine core, to the LUMO, which, apart from the expected contribution on the peripheral carbon and central nitrogen atoms of the heptazine core (see Fig. 1, right), shows a non-negligible contribution from the sulfur atoms. The S_{26} and S_{27} states, on the other hand, involve transitions from HOMO−6 and HOMO−9, which have a bigger contribution from the π-bonding electron density of the phenyl rings, to LUMO+1 and LUMO+2, which are not as clearly defined on the heptazine ring as the LUMO.

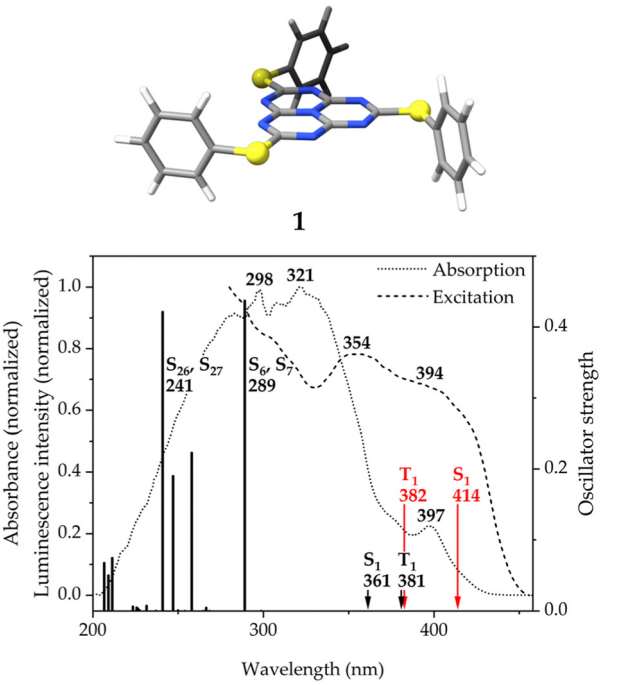

Fig. 6 (Top) The molecular structure of molecule **1** optimized at the DFT/PBE0-D3(BJ)/def2-TZVP level of theory. (Bottom) Overlay of the solid-state absorption (dotted line) and excitation (dashed line) spectra of molecule **1** with the energetically-lowest symmetry-allowed vertical singlet transitions of molecule **1** (black bars) calculated at the TD-DFT level of theory. The excitation energies of the S_1 and T_1 states calculated at the TD-DFT (black arrows) and ADC(2) (red arrows) levels of theory are also included.

Table 2 Selected vertical excitation energies (in nm [eV]), oscillator strengths (*f*, dimensionless), and orbital contributions, calculated at the TD-DFT/PBE0/def2-TZVP and ADC(2)/def2-TZVP levels of theory for molecule **1**

Transition	Irrep[a]	Energy	*f*	Contributions (%)
TD-DFT/PBE0 level of theory				
$S_1 \leftarrow S_0$	a′	361 [3.437]	0.00	37a″ → 38a″ (97.0)
$S_6 \leftarrow S_0$	a′	289 [4.290]	0.44	36a″ → 38a″ (98.4)
$S_7 \leftarrow S_0$	a′	289 [4.290]	0.44	35a″ → 38a″ (98.4)
$S_{26} \leftarrow S_0$	a′	241 [5.139]	0.42	34a″ → 39a″ (67.7)
				31a″ → 39a″ (12.0)
$S_{27} \leftarrow S_0$	a′	241 [5.146]	0.42	34a″ → 40a″ (67.7)
				31a″ → 40a″ (12.0)
$T_1 \leftarrow S_0$	a′	381 [3.251]	—	37a″ → 38a″ (97.2)
ADC(2) level of theory				
$S_1 \leftarrow S_0$	a′	414 [2.993]	0.00	37a″ → 38a″ (50.1)
				34a″ → 38a″ (44.5)
$T_1 \leftarrow S_0$	a′	382 [3.246]	—	37a″ → 38a″ (51.8)
				34a″ → 38a″ (45.7)

[a] Irreducible representation.

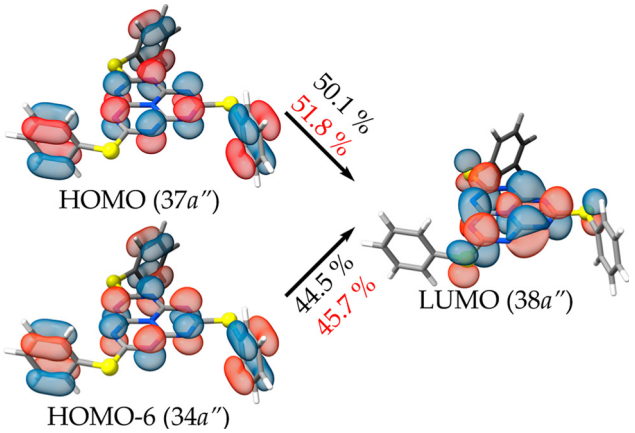

Fig. 7 Molecular orbitals and their contributions to the S_1 (T_1 in red) transition calculated at the ADC(2)/def2-TZVP level of theory for molecule **1**.

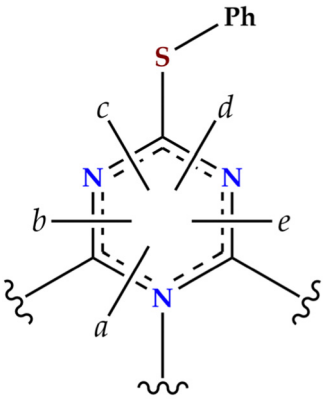

Fig. 8 Selected cut planes for the calculation of the MIC of molecule **1**.

The S_1 and T_1 states calculated at the ADC(2) level consist of the two transitions of similar weight from the HOMO and HOMO-6 to the LUMO that are depicted in Fig. 7. The spatial distribution of the HOMO and HOMO−6 is identical, with only a variation of the sign of the orbital lobes located on the peripheral nitrogen atoms of heptazine. The usual MR pattern of heptazine is accompanied by a charge transfer from a bonding π-orbital of the pending phenyl groups to an empty atomic orbital of the bridging sulfur atoms. The calculated energies at this level of theory are close to the local absorption maximum of the band edge (see Fig. 6, bottom). More importantly, the $S_1 \leftarrow S_0$ excitation energy is lower (longer wavelength) than the $T_1 \leftarrow S_0$ one, meaning that the singlet–triplet gap is inverted. The IST is consistent with the strong fluorescent property of molecule **1**.

The excitation energies to the S_1 and T_1 states have also been calculated at the complete active space self-consistent field (CASSCF) and the extended multiconfigurational quasidegenerate perturbation theory of second order (XMC-QDPT2) levels, with an active space of 6 electrons in 6 orbitals as well as with 12 electrons in 12 orbitals. The excitation energies and the singlet–triplet gaps calculated at the different levels of theory, together with the spin–orbit coupling matrix elements between S_1 and T_1 ($\langle S_1|\mathscr{H}_{SO}|T_1\rangle$) and the $S_1 \leftarrow T_1$ intersystem crossing rate constants (k_{ISC}), are collected in Table 3.

As expected, TD-DFT gives a positive IST gap. The correlated *ab initio* methods predict that the excitation energy of the $S_1 \leftarrow S_0$ transition is smaller than the $T_1 \leftarrow S_0$ transition leading to a negative singlet–triplet gap. In fact, the ΔE_{ST} of -3305 cm^{-1} obtained at the XMC-QDPT2(12,12) level is large despite the excited singlet and triplet states have the same orbital composition, suggesting a noticeable dynamic spin polarization effect. However, the excitation energies calculated at the XMC-QDPT2 level are for some unclear reason much smaller than the ones calculated at other levels of theory and too small as compared to the energy of the emitted light of 21 790 cm^{-1} corresponding to a wavelength of 459 nm. The excitation energies calculated the CASSCF level are rather independent of the size of the active space and in fair agreement with those calculated at other levels of theory and with the experimental value. The SOC matrix element between T_1 and S_1 is 0.15 cm^{-1} at the CASSCF(12,12) level yielding a k_{ISC} of the order of 10^6 s^{-1}, which is fast enough to direct the excitons to the fluorescing S_1 state. The calculated phosphorescence rate constant from T_1 to S_0 is 400 s^{-1} at the CC2 level. The calculated rate constant for the reverse ISC (k_{RISC}) from S_1 to T_1 is 0.07 s^{-1} at the XCM-DQPT2(12,12) level. These rate constants are several orders of magnitude smaller than the k_{ISC} rate constant from T_1 to S_1 of 5.5×10^5 s^{-1}, which was calculated at the XMC-QDPT2(12,12) level, the internal conversion rate constant (k_{IC}) from S_1 to S_0 is 4.0×10^4 s^{-1}, and the experimental fluorescence rate constant (k_{fluor}) from S_1 to S_0 is 3.1×10^5 s^{-1} implying that practically all excitons reach S_1 where they decay to S_0 either by fluorescence or non-radiatively through internal conversion.

2.3.2 GIMIC calculations. The (anti)aromatic character and electron delocalization pathways of molecule **1** have been

Table 3 The first vertical excitation energies, singlet–triplet gaps, and spin–orbit coupling matrix elements, calculated at the TD-DFT/PBE0/def2-TZVP, ADC(2)/def2-TZVP, CASSCF/6-31G** and XMC-QDPT2/6-31G** levels of theory for molecule **1**. Energies are given in cm^{-1} and rate constants are given in s^{-1}

Method	$E(S_1 \rightarrow S_0)$	$E(T_1 \rightarrow S_0)$	ΔE_{ST}	$\langle S_1\|\mathscr{H}_{SO}\|T_1\rangle$	k_{ISC}
TD-DFT/PBE0	27 720	26 218	+1502	—	—
ADC(2)	24 141	26 181	−2040	—	—
CASSCF(6,6)	22 818	25 714	−2896	0.16	1.0×10^6
XMC-QDPT2(6,6)	14 900	17 184	−2284	0.16	2.5×10^6
CASSCF(12,12)	22 805	25 688	−2883	0.15	1.0×10^6
XMC-QDPT2(12,12)	11 770	15 075	−3305	0.15	5.5×10^5

Table 4 The strength of the diatropic, paratropic and the net MIC (in nA T^{-1}) that pass through the integration planes shown in Fig. 8

Plane	Net	Diatropic	Paratropic
a	0.03	6.00	−5.97
b	−0.35	7.09	−7.45
c	−0.43	7.73	−8.16
d	−0.41	7.72	−8.13
e	−0.34	7.10	−7.44

investigated with the gauge-including magnetically induced currents (GIMIC) method.[41–43] The magnetically induced current (MIC) strength in the zero-field limit is determined by numerical integration of the current flowing through cut planes. The sign and the strength of the MIC distinguish between aromatic (MIC > 0 nA T^{-1}), antiaromatic (MIC < 0 nA T^{-1}), or non-aromatic (MIC ∼ 0 nA T^{-1}) molecules according to the magnetic criterion.

Previous spectroscopic studies suggested that pristine heptazine is aromatic because it has the δ (^{1}H) signal at 8.3 ppm[44] and that cyclazine (9*b*-azaphenalene) is antiaromatic, with δ (^{1}H) signals at 2.1–3.7 ppm.[45–47] In the latter, the central nitrogen atom does not participate in the π-conjugation, leading to a rim consisting of a 12π-electron annulene.

We have performed MIC calculations with the GIMIC method and integrated the strength of the MIC passing through selected cut planes as shown in Fig. 8. The profiles of the MIC passing through the cut planes are depicted in Fig. S11 (ESI†). The integrated MIC strengths of molecule **1** are collected in Table 4. The GIMIC calculations show that molecule **1** is non-aromatic, with a very weak paratropic current of *ca.* −0.4 nA T^{-1} circulating around the edge of the molecule. Visualization of the streamlines of the current-density pathways reveals that the MIC consists of small local independent vortices at the nitrogen and sulfur atoms (Fig. S12, ESI†), with hardly any current density circulating around the carbon atoms. The global non-aromaticity of the heptazine core in **1** is thus a consequence of the alternation of carbon and nitrogen atoms along the external rim that precludes free electron circulation.

2.3.3 Effect of the bridging chalcogen atom. Inspired by the potential of molecule **1** to exhibit an inverted singlet–triplet gap, we also computationally studied properties of the lowest excited states of analogues to **1**, where the sulfur atoms are replaced with the other chalcogen atoms.

The structural optimization at the DFT/PBE0-D3(BJ)/def2-TZVP level of theory of molecules **2–4** preserves, in the four cases, the three-fold symmetry of the starting C_{3h} point group of molecule **1** as extracted from its X-ray crystal structure (see Fig. 9). For molecule **4**, the σ_h plane is lost due to the torsion of the bulkier phenyltellurol groups. A selection of bond distances and angles of the optimized molecular structures of **1–4** is compared in the ESI,† with the existing X-ray structural data.[39,48] There is no experimental evidence of molecule **4**, probably due to the instability of tellurols. The agreement between the available experimental and calculated distances and angles is excellent, validating the use of the computed models for further simulations.

Table 5 The energetically lowest vertical excitation energies (in eV) and orbital contributions of molecules **2–4** calculated at the ADC(2)/def2-TZVP level of theory

Molecule	Irrep[a]	$E(S_1 \leftarrow S_0)$	Contributions (%)		$E(T_1 \leftarrow S_0)$	Contributions (%)	
2	a′	3.494	31a″ → 35a″	(72.4)	3.787	31a″ → 35a″	(74.3)
			34a″ → 35a″	(21.4)		34a″ → 35a″	(22.5)
3	a′	2.920	41a″ → 47a″	(49.7)	3.166	41a″ → 47a″	(52.1)
			46a″ → 47a″	(40.3)		46a″ → 47a″	(41.6)
4	a	3.272	140a → 141a	(84.0)	3.164	140a → 141a″	(81.1)

[a] Irreducible representation.

The vertical excitation energies to the S_1 and T_1 states have been calculated at the ADC(2) level of theory. The results are summarized in Tables 5 and 6. The orbital contributions to the most intense transitions are plotted in the ESI.†

The chemical identity of the bridging chalcogen atom has an important effect on the calculated ΔE_{ST}, which becomes smaller upon increasing the atomic number in the series **2** (X═O) > **1** (X═S) > **3** (X═Se) > **4** (X═Te). In the extreme case of molecule **4**, ΔE_{ST} is even positive. The reason for this may be found in the values of the vertical excitation energies and the orbital contributions. For molecules **1–3**, for which ΔE_{ST} is predicted to be negative, there are two main contributions to the vertical transitions, regardless of the multiplicity of the arriving state. These are analogous to the ones calculated at the same level of theory for molecule **1** (*vide supra*). The occupied MOs at Se and Te contribute to the exciton of the S_1 and T_1 states, whereas for the O and S containing molecules they do not. Since Te is larger than O, S and Se the exciton is significantly localized to Te, whereas for the three other molecules the exciton is mainly at the heptazine moiety.

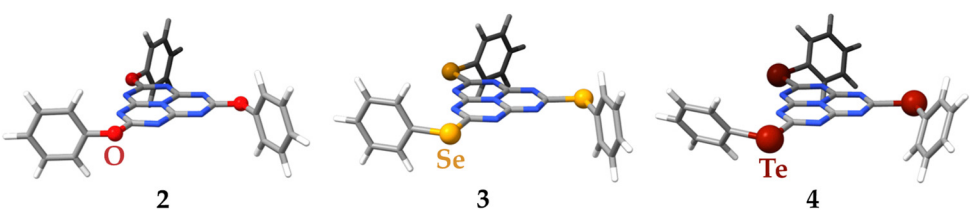

Fig. 9 The molecular structures of molecules **1–4** optimized at the DFT/PBE0-D3(BJ)/def2-TZVP level of theory.

Table 6 The first vertical excitation energies and the obtained singlet–triplet gap, calculated at the ADC(2)/def2-TZVP level of theory for molecules **2–4**. All values are given in eV

Molecule	Irrep[a]	$E(S_1 \leftarrow S_0)$	$E(T_1 \leftarrow S_0)$	ΔE_{ST}
2	a′	3.494	3.787	−0.293
3	a′	2.920	3.166	−0.246
4	a′	3.272	3.164	+0.108

[a] Irreducible representation.

3 Conclusions

The three-fold symmetrical 2,5,8-tris(phenylthiolato)heptazine molecule (**1**) emits in blue at 459 nm with an emission lifetime of 462 ns and 171 ns, and a PLQY of 0.71 and 0.33, in toluene solution and in the solid state, respectively. The complete overlap of the excitation spectrum with the absorption one, the relatively short lifetimes, and the insensitivity of the emission spectral profile to the presence of dissolved oxygen are indicative of the emission having fluorescent character. The collected photophysical data are not conclusive of an inversion of the first excited states of molecule **1**. However, since no emission from an excited triplet state could be detected, this unequivocally demonstrates that the emissive state is of singlet multiplicity. S_1 is also the only state from which photoluminescence should be expected for an IST molecule under ambient conditions. Correlated *ab initio* level calculations show that **1** has a large inverted singlet–triplet energy splitting of $-2883\ cm^{-1}$ (−0.36 eV) at the CASSCF(12,12) level, which is not obtained in TD-DFT calculations. The calculated spin–orbit coupling matrix element between S_1 and T_1 of $0.15\ cm^{-1}$ yields a k_{ISC} of $10^6\ s^{-1}$ between the T_1 and S_1 states. The relaxation of the excitons directs them to the emitting S_1 state leading to the strong luminescence.

This study demonstrates the potential of three-fold symmetric ether, thioether, and selenoether derivatives of heptazine to also be among the fifth generation of emitter molecules. Further efforts will be devoted to the synthesis of new analogs of molecule **1** and its implementation in working OLED devices.

4 Experimental

4.1 General procedures

(DR)-UV-Vis spectra were measured in a Shimadzu UV-3600 spectrophotometer. For the collection of DR-UV-vis spectra, a Harrick Praying Mantis diffuse reflection accessory was employed. For the collection of UV-vis spectra, Hellma Quartz Suprasil cells with an optical path of 1 cm were employed. Temperature was controlled with a Shimadzu TCC-240A cell holder. Photoluminescence spectra were measured in an Edinburgh Instruments FLS 1000 spectrofluorimeter. Emission lifetimes were determined with the time-correlated single photon counting (TCSPC) technique employing Edinburgh Instruments EPL-375 (λ_{ex} of 375 nm) and EPL-295 (λ_{ex} of 295 nm) picosecond pulsed diode lasers as the excitation source. The transient photoluminescence decay data was fitted to a model function of one to three exponential parameters

$$I(t) = A + \sum_{1}^{n} B_i \cdot \exp\left(\frac{t}{\tau_i}\right) \quad (1)$$

where A, B_i and τ_i are fitting parameters, and n is an integer between 1 and 3 optimized to improve the quality of the fitting as given by the value of χ^2. The average emission lifetime ($\langle\tau\rangle_{amp}$) is obtained as

$$\langle\tau\rangle_{amp} = \frac{\sum_i (B_i \cdot \tau_i)}{\sum_i B_i} \quad (2)$$

Absolute photoluminescence quantum yields were determined with a Hamamatsu Quantaurus-QY C11347 instrument. HPLC grade toluene was degassed and dried with a MBRAUN MB-SPS800 system. The solutions for photophysical measurements were prepared inside a MBRAUN LABstar glovebox under Ar atmosphere. For measurements in the presence of oxygen, air was bubbled through the neat solvent for 10 min.

4.2 Synthesis of 2,5,8-tris(phenylthiolato)heptazine (1)

2,5,8-Tris(phenylthiolato)heptazine (**1**) was prepared employing standard Schlenk techniques from 2,5,8-trichloroheptazine[49] and excess phenylthiol (Sigma-Aldrich) following a previously reported method,[39] but employing anhydrous toluene instead of mesitylene as the solvent, and purifying the solid product by flash column chromatography (8 dichloromethane:2 *n*-hexane).[3]

4.3 Computational details

The calculations were carried out using TURBOMOLE version 7.5.1.[50,51] The starting geometry of molecule **1** was extracted from its X-ray structure[39] and employed as a template for molecules **2–4**. The structures were optimized at the density functional theory (DFT) level[52] with the PBE0 functional,[53–55] def2-TZVP basis sets on all atoms,[56] the resolution-of-the-identity (RI) approximation,[57–59] and the D3(BJ) semiempirical correction to dispersion interactions.[60,61] The models were verified as minima by the analytical computation of the vibrational frequencies.[62] The first vertical singlet and triplet excitation energies were calculated at the algebraic diagrammatic construction of second order [ADC(2)] level[35] with def2-TZVP basis sets on all atoms.[56] The optimized molecular structures, orbitals, and exciton surfaces were visualized and rendered using UCSF ChimeraX version 1.5.[63] Excitation energies were calculated with the Firefly program at the state-averaged complete active space self-consistent field (CASSCF) level with the active space consisting of 6 electrons in 6 orbitals as well as with 12 electrons in 12 orbitals[64,65] They were also calculated at the extended multiconfigurational quasi degenerate perturbation theory at the second order (XMC-QDPT2) level[64,65] using the same active spaces. The matrix element of the one-electron spin–orbit coupling operator ($\mathscr{H}_{SO}$) between the T_1 and S_1 states ($\langle S_1|\mathscr{H}_{SO}|T_1\rangle$) was calculated at the CASSCF levels using GAMESS-US.[66] The k_{ISC} rate constant (in s^{-1}) for the $S_1 \leftarrow T_1$

transition was calculated using[67]

$$k_{\mathrm{ISC}} = 1.6 \times 10^{9} \cdot \langle \mathrm{S}_1 | \mathscr{H}_{\mathrm{SO}} | \mathrm{T}_1 \rangle^2 \cdot \left(\sum_{n_1,\ldots,n_{3N-6}}^{\mathrm{Comb}} \prod_{k=1}^{3N-6} \sqrt{\frac{\exp(-y_k) \cdot y_k^{n_k}}{n_k!}} \right)^2, \quad (3)$$

where y_k is the Huang–Rhys factor and n_k is the vibrational quantum number of the kth-promoting vibrational mode.[68] In eqn (3), Comb denotes all combinations of vibrational modes that fulfill the energy conservation condition.

The magnetically induced current (MIC) densities were calculated using the gauge-including magnetically induced currents (GIMIC) method.[41–43] Ring-current strength susceptibilities, which are denoted ring-current strengths, were obtained by numerical integration of the current density passing through a cut-plane perpendicular to a selected bond. The current density was calculated at the BHandHLYP/def2-TZVP level of theory (LIBXC ID 436).[69–71]

Author contributions

J. M. L., M. M., R. R. V., and D. S. acquired funding. J. M. L. and M. M. provided experimental resources. D. S. provided computational resources. D. B. did the experimental work and the calculations at the DFT, TD-DFT and ADC(2) levels of theory. R. T. N. and R. R. V. did the calculations at the CASSCF and XMC-QDPT2 levels of theory. D. B. did the MIC calculations with the GIMIC method. D. B. and D. S. wrote the first version of the manuscript. All authors contributed to the final version of the manuscript.

Conflicts of interest

There are no conflicts to declare.

Acknowledgements

The research has been supported by the Spanish D. G. I. MINECO/FEDER (project number PID2022-139739NB-00I, AEI/FEDER, UE) and by The Academy of Finland (project numbers 340582 and 340583). DB acknowledges Universidad de La Rioja for the concession of a Margarita Salas postdoc fellowship financed by the Spanish Ministerio de Universidades and the European Union-NextGenerationEU program.

References

1 P. Audebert, E. Kroke, C. Posern and S.-H. Lee, *Chem. Rev.*, 2021, **121**, 2515–2544.
2 D. M. Mayder, C. M. Tonge, G. D. Nguyen, R. Hojo, N. R. Paisley, J. Yu, G. Tom, S. A. Burke and Z. M. Hudson, *Chem. Mater.*, 2022, **34**, 2624–2635.
3 L. Galmiche, C. Allain, T. Le, R. Guillot and P. Audebert, *Chem. Sci.*, 2019, **10**, 5513–5518.
4 J. Li, H. Nomura, H. Miyazaki and C. Adachi, *Chem. Commun.*, 2014, **50**, 6174–6176.
5 J. Li, Q. Zhang, H. Nomura, H. Miyazaki and C. Adachi, *Appl. Phys. Lett.*, 2014, **105**, 013301.
6 J. Li, T. Nakagawa, J. MacDonald, Q. Zhang, H. Nomura, H. Miyazaki and C. Adachi, *Adv. Mater.*, 2013, **25**, 3319–3323.
7 J. Ehrmaier, E. J. Rabe, S. R. Pristash, K. L. Corp, C. W. Schlenker, A. L. Sobolewski and W. Domcke, *J. Phys. Chem. A*, 2019, **123**, 8099–8108.
8 D. Blasco, R. T. Nasibullin, R. R. Valiev and D. Sundholm, *Chem. Sci.*, 2023, **14**, 3873–3880.
9 P. de Silva, C. A. Kim, T. Zhu and T. Van Voorhis, *Chem. Mater.*, 2019, **31**, 6995–7006.
10 N. Aizawa, Y.-J. Pu, Y. Harabuchi, A. Nihonyanagi, R. Ibuka, H. Inuzuka, B. Dhara, Y. Koyama, K.-I. Nakayama, S. Maeda, F. Araoka and D. Miyajima, *Nature*, 2022, **609**, 502–506.
11 G. Ricci, J.-C. Sancho-García and Y. Olivier, *J. Mater. Chem. C*, 2022, **10**, 12680–12698.
12 L. Tučková, M. Straka, R. R. Valiev and D. Sundholm, *Phys. Chem. Chem. Phys.*, 2022, **24**, 18713–18721.
13 J. Li, Z. Li, H. Liu, H. Gong, J. Zhang, X. Li, Y. Wang and Q. Guo, *Dyes Pigm.*, 2022, **203**, 110366.
14 S. Ghosh and K. Bhattacharyya, *J. Phys. Chem. A*, 2022, **126**, 1378–1385.
15 F. Dinkelbach, M. Bracker, M. Kleinschmidt and C. M. Marian, *J. Phys. Chem. A*, 2021, **125**, 10044–10051.
16 S. Pios, X. Huang, A. L. Sobolewski and W. Domcke, *Phys. Chem. Chem. Phys.*, 2021, **23**, 12968–12975.
17 R. Pollice, P. Friederich, C. Lavigne, G. dos Passos Gomes and A. Aspuru-Guzik, *Matter*, 2021, **4**, 1654–1682.
18 K. Bhattacharyya, *Chem. Phys. Lett.*, 2021, **779**, 138827.
19 A. L. Sobolewski and W. Domcke, *J. Phys. Chem. Lett.*, 2021, **12**, 6852–6860.
20 J. Sanz-Rodrigo, G. Ricci, Y. Olivier and J. C. Sancho-García, *J. Phys. Chem. A*, 2021, **125**, 513–522.
21 G. Ricci, E. San-Fabián, Y. Olivier and J. C. Sancho-García, *ChemPhysChem*, 2021, **22**, 553–560.
22 P. de Silva, *J. Phys. Chem. Lett.*, 2019, **10**, 5674–5679.
23 F. Hund, *Zeitschrift für Physik*, 1925, **33**, 345–371.
24 S. Koseki, T. Nakajima and A. Toyota, *Can. J. Chem.*, 1985, **63**, 1572–1579.
25 M. H. Garner, J. T. Blaskovits and C. Corminboeuf, *Chem. Sci.*, 2023, **14**, 10458–10466.
26 J. T. Blaskovits, M. H. Garner and C. Corminboeuf, *Angew. Chem., Int. Ed.*, 2023, **62**, e202218156.
27 M. E. Sandoval-Salinas, G. Ricci, A. J. Pérez-Jiménez, D. Casanova, Y. Olivier and J. C. Sancho-García, *Phys. Chem. Chem. Phys.*, 2023, **25**, 26417–26428.
28 J. Li, Z. Li, H. Liu, H. Gong, J. Zhang, Y. Yao and Q. Guo, *Front. Chem.*, 2022, **10**, 999856.
29 T. Won, K.-I. Nakayama and N. Aizawa, *Chem. Phys. Rev.*, 2023, **4**, 021310.
30 H. Kollmar and V. Staemmler, *Theor. Chim. Acta*, 1978, **48**, 223–239.

31 W. T. Borden and E. R. Davidson, *J. Am. Chem. Soc.*, 1977, **99**, 4587–4594.
32 W. T. Borden, *J. Am. Chem. Soc.*, 1975, **97**, 5968–5970.
33 O. Christiansen, H. Koch and P. Jørgensen, *Chem. Phys. Lett.*, 1995, **243**, 409–418.
34 C. Hättig and F. Weigend, *J. Chem. Phys.*, 2000, **113**, 5154–5161.
35 C. Hättig, *Adv. Quantum Chem.*, 2005, **50**, 37–60.
36 A. Dreuw and M. Wormit, *Wiley Interdiscip. Rev.: Comput. Mol. Sci.*, 2015, **5**, 82–95.
37 A. Dreuw and M. Head-Gordon, *Chem. Rev.*, 2005, **105**, 4009–4037.
38 Ö. H. Omar, X. Xie, A. Troissi and D. Padula, *J. Am. Chem. Soc.*, 2023, **145**, 19790–19799.
39 C. Posern, U. Böhme, J. Wagler, C.-C. Höhne and E. Kroke, *Chem. – Eur. J.*, 2017, **23**, 12510–12518.
40 B. Valeur and M. N. Berberan-Santos, *Molecular Fluorescence: Principles and Applications*, John Wiley & Sons, Ltd, 2012, ch. 6, pp. 141–179.
41 J. Jusélius, D. Sundholm and J. Gauss, *J. Chem. Phys.*, 2004, **121**, 3952–3963.
42 D. Sundholm, H. Fliegl and R. J. Berger, *Wiley Interdiscip. Rev.: Comput. Mol. Sci.*, 2016, **6**, 639–678.
43 GIMIC, version 2.0, a current density program, Can be freely downloaded from **https://github.com/qmcurrents/gimic** and **https://zenodo.org/record/8180435**.
44 R. S. Hosmane, M. A. Rossman and N. J. Leonard, *J. Am. Chem. Soc.*, 1982, **104**, 5497–5499.
45 D. Farquhar and D. Leaver, *J. Chem. Soc., D*, 1969, 24–25.
46 C. Trujillo, G. Sánchex-Sanz, I. Alkorta and J. Elguero, *Struct. Chem.*, 2017, **28**, 345–355.
47 E. Kleinpeter and A. Koch, *Eur. J. Org. Chem.*, 2022, e202101362.
48 M. R. Schwarz, H. Ehrenberg, M. A. Kloc and E. Kroke, *Heterocycles*, 2006, **68**, 2499–2507.
49 E. J. Rabe, K. L. Corp, A. L. Sobolewski, W. Domcke and C. W. Schlenker, *J. Phys. Chem. Lett.*, 2018, **9**, 6257–6261.
50 S. G. Balasubramani, G. P. Chen, S. Coriani, M. Diedenhofen, M. S. Frank, Y. J. Franzke, F. Furche, R. Grotjahn, M. E. Harding, C. Hättig, A. Hellweg, B. Helmich-Paris, C. Holzer, U. Huniar, M. Kaupp, A. Marefat Khah, S. Karbalaei Khani, T. Müller, F. Mack, B. D. Nguyen, S. M. Parker, E. Perlt, D. Rappoport, K. Reiter, S. Roy, M. Rückert, G. Schmitz, M. Sierka, E. Tapavicza, D. P. Tew, C. van Wüllen, V. K. Voora, F. Weigend, A. Wodynski and J. M. Yu, *J. Chem. Phys.*, 2020, **152**, 184107.
51 TURBOMOLE V7.5.1 2021, a development of University of Karlsruhe and Forschungszentrum Karlsruhe GmbH, 1989–2007, TURBOMOLE GmbH, since 2007; available from **https://www.turbomole.org** (accessed 25.10.2022).
52 O. Treutler and R. Ahlrichs, *J. Chem. Phys.*, 1995, **102**, 346–354.
53 J. P. Perdew, K. Burke and M. Ernzerhof, *Phys. Rev. Lett.*, 1996, **77**, 3865.
54 J. P. Perdew and M. Ernzerhof, *J. Chem. Phys.*, 1996, **105**, 9982.
55 C. Adamo and V. Barone, *J. Chem. Phys.*, 1999, **110**, 6158–6170.
56 F. Weigend and R. Ahlrichs, *Phys. Chem. Chem. Phys.*, 2005, **7**, 3297–3305.
57 K. Eichkorn, O. Treutler, H. Öhm, M. Häser and R. Ahlrichs, *Chem. Phys. Lett.*, 1995, **242**, 652–660.
58 K. Eichkorn, F. Weigend, O. Treutler and R. Ahlrichs, *Theor. Chem. Acc.*, 1997, **97**, 119–124.
59 F. Weigend, *Phys. Chem. Chem. Phys.*, 2006, **8**, 1057–1065.
60 S. Grimme, J. Antony, S. Ehrlich and H. Krieg, *J. Chem. Phys.*, 2010, **132**, 154104.
61 S. Grimme, S. Ehrlich and L. Goerigk, *J. Comput. Chem.*, 2011, **32**, 1456–1465.
62 P. Deglmann, K. May, F. Furche and R. Ahlrichs, *Chem. Phys. Lett.*, 2004, **384**, 103–107.
63 E. F. Pettersen, T. D. Goddard, C. C. Huang, E. C. Meng, G. S. Couch, T. I. Croll, J. H. Morris and T. E. Ferrin, *Protein Sci.*, 2021, **30**, 70–82.
64 A. A. Granovsky, *Firefly version 8.0.0*, **https://classic.chem.msu.su/gran/firefly/index.html** (accessed 30.9.2023).
65 A. A. Granovsky, *J. Chem. Phys.*, 2011, **134**, 214113.
66 M. W. Schmidt, K. K. Baldridge, J. A. Boatz, S. T. Elbert, M. S. Gordon, J. H. Jensen, S. Koseki, N. Matsunaga, K. A. Nguyen, S. Su, T. L. Windus, M. Dupuis and J. A. Montgomery, *J. Comput. Chem.*, 1993, **14**, 1347–1363.
67 R. R. Valiev, B. S. Merzlikin, R. T. Nasibullin, A. Kurtzevitch, V. N. Cherepanov, R. R. Ramazanov, D. Sundholm and T. Kurtén, *Phys. Chem. Chem. Phys.*, 2023, **25**, 6406–6415.
68 R. R. Valiev, V. N. Cherepanov, G. V. Baryshnikov and D. Sundholm, *Phys. Chem. Chem. Phys.*, 2018, **20**, 6121–6133.
69 A. D. Becke, *Phys. Rev. A: At., Mol., Opt. Phys.*, 1988, **38**, 3098–3100.
70 A. D. Becke, *J. Chem. Phys.*, 1993, **98**, 1372–1377.
71 S. Lehtola, C. Steigemann, M. J. Oliveira and M. A. Marques, *SoftwareX*, 2018, **7**, 1–5.